High-performance dual-mode ultra-thin broadband CdS/CIGS heterojunction photodetector on steel

XI ZENG,^{1,*} D JACKSON LONTCHI,¹ MARIA ZHUKOVA,¹ PIETER BOLT,² MARCEL SMOR,² LIONEL FOURDRINIER,³ GUOLI LI,⁴ AND DENIS FLANDRE¹

Abstract: An ultra-thin CdS/CIGS heterojunction photodiode fabricated on steel firstly exhibits dual-mode broadband photodetection from ultraviolet to near infrared spectrum. In the photovoltaic mode, the CIGS photodiode, working as a self-driven photodetector, shows an outstanding photodetection capability (under a light power density of $20 \,\mu\text{W}$ cm⁻² at $680 \,\text{nm}$), reaching a record detectivity of $\sim 4.4 \times 10^{12}$ Jones, a low noise equivalent power (*NEP*) of $0.16 \,\text{pW}$ Hz^{-1/2} and a high I_{light}/I_{dark} ratio of $\sim 10^3$, but a relatively low responsivity of $\sim 0.39 \,\text{A}$ W⁻¹ and an external quantum efficiency (*EQE*) of $\sim 71\%$. Working under the same illumination but in the photoconductive mode (1 V reverse bias), the responsivity and *EQE* are significantly enhanced to $1.24 \,\text{A}$ W⁻¹ and 226%, respectively, but with a relatively low detectivity of 7×10^{10} Jones and a higher *NEP* of $10.1 \,\text{pW}$ Hz^{-1/2}. To explain these results, a corrected photoconductive gain (*G*) model indicates that minority electrons could be localized in the defects, surface states and depletion region of the CIGS photodiode, causing excess hole accumulation in the ultra-thin CIGS photodiode and thus high *EQE* over 100% (*G* over 1).

© 2022 Optica Publishing Group under the terms of the Optica Open Access Publishing Agreement

1. Introduction

Large-area broadband photodetection from ultraviolet to infrared regime is of interest in various applications, including imaging, spectroscopy, optical communication, environmental monitoring and chemical or biological sensing [1,2]. Photodetectors normally work either in a photovoltaic mode without an external bias or in a photoconductive mode with an external bias. In the photovoltaic mode, a self-driven photodetector usually demonstrates high detectivity for weak signal detection [3]. However, its external quantum efficiency (*EQE*) is theoretically below 100%, which also limits the responsivity. Conversely, in the photoconductive mode, the responsivity is significantly enhanced thanks to the external bias and the improved charge collection efficiency [4,5]. However, the illumination to dark current ratio and the detectivity are sacrificed in this mode due to the rising dark current. Besides, conventional photodetectors working in the photoconductive mode consumes external energy, while self-driven photodetectors working in the photovoltaic mode can sustainably operate as individual sensors in harsh environments without external energy consumption [3,6]. Therefore, dual-mode photodetectors, which can dynamically switch operation modes, show their potential to realize high detectivity and responsivity simultaneously in a single device [7].

¹Institute of Information and Communication Technologies, Electronics and Applied Mathematics, Université Catholique de Louvain, Louvain-la-Neuve 1348, Belgium

²TNO, Department of Solar Technology and Applications, High Tech Campus 21, Eindhoven 5656 AE, Netherlands

³AC&CS – CRM Group, Boulevard de Colonster B57, Liege 4000, Belgium

⁴School of Physics and Electronics, Hunan University, Changsha 410082, China

^{*}xi.zeng@uclouvain.be

As a high-efficient p-type semiconductor used in photovoltaic applications, Cu(In,Ga)Se₂ (CIGS) possesses the capability to be used as a light absorbing material in broadband ultra-thin photodetectors covering the visible spectrum owing to its tunable direct bandgap (1.04-1.67 eV), high absorption coefficient (>10⁵ cm⁻¹) and outstanding stability [8,9]. However, CIGS-based photodetectors have barely been studied up to date. Among various structures, CdS/CIGS heterojunctions were proved to be mature structures for photodetection [9–11]. Working in the photoconductive mode, CdS/CIGS heterojunction photodiodes were firstly studied for broadband photodetection [10] and improved by potassium incorporation specifically for the near infrared (NIR) photodetection [11]. Working in the photovoltaic mode as self-driven photodetectors, CdS/CIGS heterojunction photodiodes were improved by Al₂O₃ passivation [9]. In this mode, CdS/CIGS heterojunctions were also used to fabricate self-driven optical position sensitive detectors (PSD) thanks to a lateral photovoltaic effect [12,13]. However, these CdS/CIGS photodetectors with thick CIGS layers over 1 µm, focused either on a single mode, or on a specifically narrow band photodetection. In our previous research, dual-mode broadband photodetection was developed in an ultra-thin In₂S₃/CIGS heterojunction with CIGS thickness of 800 nm, reaching a record responsivity of 2.06 A W^{-1} or a detectivity of 3.4×10¹² Jones under 870 nm illumination in the photovoltaic or photoconductive modes, respectively [14]. Several CIGS photodiodes have shown EOE > 100% under high bias, which was explained by a classical photoconductive gain mechanism caused by photogenerated carrier recirculation and hole injection [11,14]. However, this hypothesis is problematic because hole injection appears both in the dark and under illumination if this injection is caused by the band bending from external bias. Both light and dark currents would thus increase, but it's questioned whether the injection gets stronger when the device is illuminated.

Fabricating photodetectors on flexible substrates is of great interest because roll-to-roll deposition methods can be implemented to lower the manufacturing cost compared to traditional batch-to-batch or in-line methods on rigid glass substrates [15]. As a well-known promising flexible substrate, the low-cost stainless-steel foil is used in this work because of its commercial availability, mechanically stability, and resistance to high temperature [16,17]. However, flexible substrates cannot provide alkaline doping due to the lack of alkaline elements compared to standard rigid substrates like soda lime glass substrates. Soda lime glass substrates are indeed considered as mature substrates to provide the diffusion of alkaline elements like Na and K through the Mo back electrode into CIGS during the CIGS growth [18]. The doping from alkaline elements can passivate the defects at CIGS surface, increase the hole concentration in CIGS absorber and thus contribute to a higher free carrier density used for photoresponse [19–21]. To provide alkaline elements on flexible substrates, an 8 nm thick NaF precursor is deposited prior to CIGS evaporation.

Herein, dual-mode operation of an ultra-thin AZO/ZnO/CdS//CIGS/Mo heterojunction photodiode on low-carbon steel substrate is firstly realized in broadband photodetection from UV to near-infrared spectrum (375-910 nm) both in the photovoltaic mode as a self-driven photovoltaic detector and in the photoconductive mode as a photoconductive detector. The CIGS thickness is firstly reduced to 750 nm for CdS/CIGS heterojunction photodetectors, which allows to fabricate commercial CIGS photodetectors in a low-cost way. The dark *I-V* and *C-V* behaviors are discussed and analyzed to help understand the CdS/CIGS heterojunction. Dual-mode broadband photodetection is demonstrated, reaching a record detectivity of $\sim 4.4 \times 10^{12}$ Jones, a low noise equivalent power (*NEP*) of 0.16 pW Hz^{-1/2} and a high I_{light}/I_{dark} ratio of over $\sim 10^3$ at 0 V, and an enhanced responsivity of 1.24 A W⁻¹ and an impressive *EQE* of 226% at 1 V reverse bias. A stable, fast, and repeatable photoresponse is obtained by switching the incident LED light, revealing a short response time below 5 ms. To understand the dark characteristics and band offsets of the CdS/CIGS photodiode, SCAPS-1D and SILVACO ATLAS-2D simulations are investigated [22,23]. To fully understand the photodetection mechanism, a corrected photoconductive gain

model is investigated for the CdS/CIGS photodiode, in comparison with the misleading classical model. These characterizations demonstrate excellent broadband photodetection abilities of the CdS/CIGS heterojunction photodiode by switching the operation modes.

2. Experimental methods

2.1. Device fabrication

The CdS/CIGS photodiode was fabricated by several groups within European H2020 ARCIGS-M project. The top layers of the CdS/CIGS photodiode were fabricated by TNO on a commercial low-carbon steel foil substrate with a top isolation layer from AC&CS in CRM group. Mo (500 nm) was DC sputtered on the steel substrate as a back ohmic contact with CIGS. After introducing an Alkali element (Na) doping from a thin NaF precursor (8 nm), CIGS (750 nm) with less defects and higher hole concentration was evaporated by a three-stage co-evaporation process. Chemical portions of Cu, In and Ga in CIGS are 22.95%, 17.72% and 9.6% respectively. CdS (50nm) buffer layer was deposited by the chemical bath deposition (CBD). Intrinsic ZnO (50 nm) and aluminum-doped ZnO (AZO) (300 nm) were sputtered as a highly resistive window layer and a low resistive contact layer, respectively. The photodetector was completed by the evaporation of Ni/Ag/Ni top contacts. The whole stack of devices was finally divided into individually contacted photodiodes (50×100 mm) by mechanical scribes.

2.2. Device characterization

The structure and morphology of the CdS/CIGS photodiode were characterized by Zeiss Auriga focused ion beam—scanning electron microscopy (FIB-SEM). The dark current-voltage(*I-V*) curve and capacitance-voltage (*C-V*) curve at 5000 Hz frequency were measured by four-point probe measurements on a low signal probe station (PM8PS) connected to Agilent B1500A Semiconductor Device Analyzer. The current-voltage (*I-V*), and time-dependent transient current (*I-T*) were measured by the same technique under the illumination of light emitting diodes (Thorlabs, LED375L-LED910L) specifically at 375, 395, 430, 450, 490, 505, 555, 590, 630, 680, 760, 810, 870, 910 nm. For the *I-V* measurements, the LEDs were powered by Keithley 2400 source meter. For the transient response measurements, the LEDs were powered by Tektronix AFG2021 Arbitrary Function Generator. The incident light densities of LEDs were measured by a power meter (Ophir Optronics, Ophir Nova 1Z01500), integrating a standard silicon photodetector PD300 with detection range from 200 to 1100 nm. A shadow mask was used to fix the effective photodetection area of the CdS/CIGS photodiode and eliminate the influence of neighbor devices. All the measurements were performed at a constant chuck temperature of 25 °C.

3. Experimental results

The schematic structure of the CdS/CIGS photodiode is shown in Fig. 1(a). A cross-section scanning electron microscope (SEM) image of the CdS/CIGS photodiode shows well prepared distinct interfaces for each layer in Fig. 1(b). Mo back-contact layer, CIGS absorber, CdS buffer layer, ZnO window layer and AZO contact layer can be seen clearly in the SEM image from bottom to top on the low-carbon steel foil substrate.

To analyze the dark characteristics of the CdS/CIGS photodiode, a single diode model, which includes a diode (D), a shunt resistance (R_{shunt}) and a series resistance (R_s) , is used to fit the dark current-voltage $(I_{dark}-V)$ and dark current density-voltage $(J_{dark}-V)$ experimental curves in Fig. 1(c). The equivalent circuit of this model was presented in [14]. In this model, each component is extracted from corresponding bias region to distinguish the different contributions

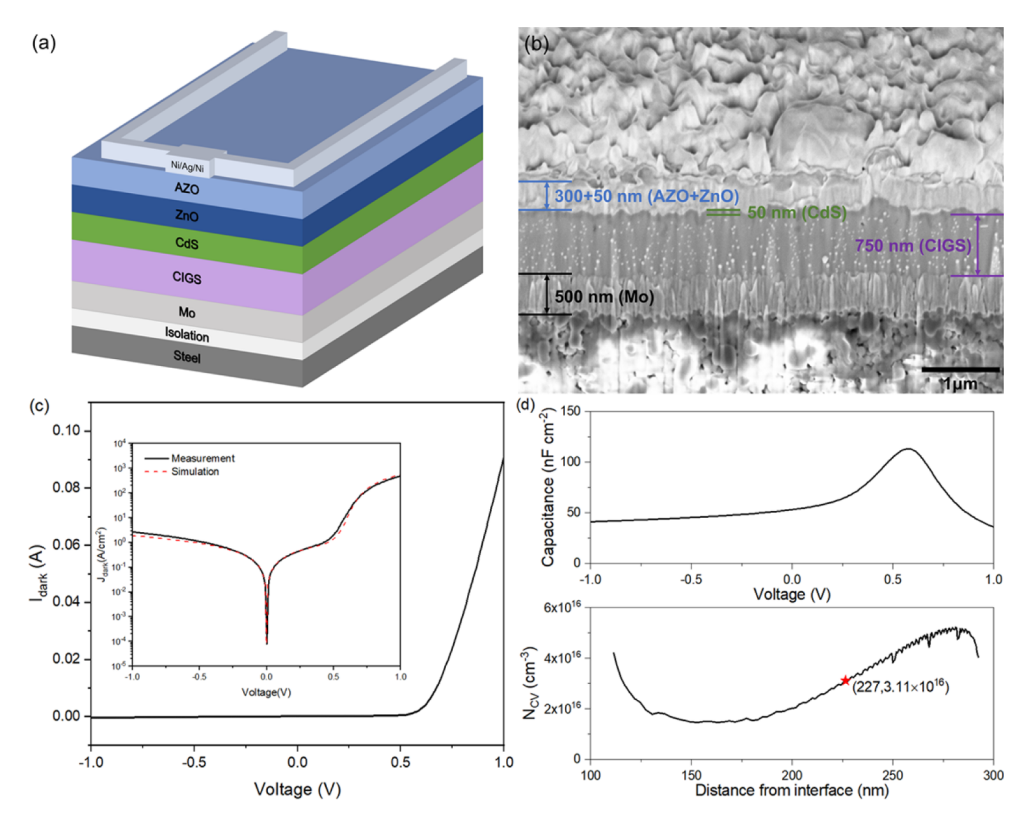


Fig. 1. (a) Schematic Structure and (b) cross-section SEM image of the CdS/CIGS photodiode. (c) Dark *I-V* curve of the CdS/CIGS photodiode (the inserts are experimental and simulated dark *J-V* curves in logarithm scale). (d) Dark C-V curve and calculated $N_{CV}-W$ curve of the CdS/CIGS photodiode.

to J_{dark} , which is modelled by:

$$J_{dark} = J_0 \left\{ exp \left[\frac{q(V - J_{dark}R_S)}{nkT} \right] - 1 \right\} + \frac{V - J_{dark}R_S}{R_{shunt}}$$
 (1)

where V is the applied voltage, q is the electron charge, k is the Boltzmann constant, and T is the temperature.

The first term of (1), extracting diffusion current parameters and R_s from high forward bias, provides good fitting between the experiment curve and the model, with J_0 of 7.33×10^{-8} A cm⁻², n of 1.86 and R_s of $0.5 \ \Omega \cdot \text{cm}^2$. The shunt leakage current is dominant under the reverse bias, and R_{shunt} is obtained from the minimum of dJ/dV [24]. The CdS/CIGS photodiode on steel shows a lower R_{shunt} of $5.33 \times 10^2 \ \Omega \cdot \text{cm}^2$, than the reported R_{shunt} from 10^3 to $10^4 \ \Omega \cdot \text{cm}^2$ for a CdS/CIGS heterojunction on glass and thus a higher dark shunt leakage current [25]. By setting the calculated R_{shunt} and R_s in SCAPS simulation [22], the dark characteristics in Fig. 1(c) reveal excellent fitting between measurement and simulation, that justifies the use of the single-diode model.

The low-frequency capacitance-voltage (C-V) curve of the CdS/CIGS photodiode is performed in the dark (Fig. 1(d)). The capacitance increases sub-linearly from reverse to low forward bias region with the decrease of depletion region depth, but exponentially when the diode current dominates. At high forward bias, the series resistance strongly impacts the capacitance measurement. From C-V curve, the net free carrier concentration (N_{CV}) and the depletion region

width (W) can both be calculated by [26]:

$$N_{CV} = \frac{-2}{q\varepsilon_0 \varepsilon A^2 [d(1/c^2)/dV]}$$
 (2)

$$W = \frac{\varepsilon_0 \varepsilon A}{C} \tag{3}$$

where ε_0 is the vacuum permittivity, ε is the CIGS dielectric constant (=13.6), and A is the device area (=0.5 cm²). In Fig. 1(d), N_{CV} is plotted against W, extracting N_{CV} of 3.11×10^{16} cm⁻³ and W of 227 nm at 0 V. Such high N_{CV} , which is close to other CIGS/CdS heterojunctions on glass, is attributed to an enhanced Na concentration from the NaF precursor [11,27]. More defects within the bandgap for CIGS fabricated on steel substrates causes a narrower W compared to CIGS/CdS heterojunctions on glass [26,27], which is consistent with high capacitance measured for the device on steel.

Next, the dual-mode broadband photodetection of the CdS/CIGS photodiode is investigated. Photoresponsivity (R), and Detectivity (D), which are two figures of merit to evaluate the photodetector sensitivity to the incident light and its ability to detect weak optical signal, are given by [28]:

$$R = \frac{I_{photo}}{PA} = \frac{I_{light} - I_{dark}}{PA} \tag{4}$$

$$D = \frac{RA_{eff}^{0.5}}{(2qI_{dark})^{0.5}} \tag{5}$$

where I_{photo} is the excited photocurrent, I_{light} is the current under illumination, I_{dark} is the current in the dark, P is the incident light density, and A_{eff} is the effective illuminated area of the photodetector (=0.5 cm²). Noise equivalent power (*NEP*), that is defined as the minimum incident optical power to produce a signal-to-noise ratio (*SNR*) of 1 in a 1 Hz bandwidth, is obtained by [29,30]:

$$NEP = \frac{I_n}{R} \approx \frac{I_{ns}}{R} = \frac{(2qI_{dark}B)^{0.5}}{R} = \frac{(A_{eff}B)^{0.5}}{D}$$
 (6)

where I_n is the total noise current, and B is the bandwidth (B is normalized as 1 Hz). In photodetectors, shot noise current (I_{ns}) from the dark current is dominant [31]. Defining B as 1 Hz, NEP of the photodetectors can be simply calculated from D [29,31]. Moreover, external quantum efficiency (EQE), which can also be described as photogain (G), is defined as the ratio of photogenerated carriers to incident photons, and obtained by [30]:

$$G = EQE = \frac{hcR}{q\lambda} \tag{7}$$

where h is the Plank constant, c is the light velocity, and λ is the incident light wavelength.

To analyze the dual-mode broadband photodetection, the spectral responsivity, EQE and detectivity of the CdS/CIGS photodiode from 375 to 910 nm illuminations of 100 μ W cm⁻² are calculated in Fig. 2(a-c) both in the photovoltaic mode (0 V bias) and photoconductive mode (1 V reverse bias). In the photovoltaic mode, high detectivities over 2×10^{12} Jones are obtained from 395 to 910 nm thanks to their negligible dark current with the absence of external bias. The maximum detectivity and minimum NEP reach 4.4×10^{12} Jones and 0.16 pW Hz^{-1/2} at 680 nm, respectively. However, the responsivities and EQEs are below 0.4 A W⁻¹ and 100%, respectively, because of low photocurrent without external bias. In contrast, in the photoconductive mode, enhanced responsivities over 0.4 A W⁻¹ are obtained from 490 to 910 nm. Meanwhile, impressive EQEs over 100% are observed from 490 to 680 nm due to the

photoconductive gain mechanism. The maximum responsivity is extracted to be 0.66 A W^{-1} at 680 nm, corresponding to a high EQE of 121%. However, the detectivities and NEPs are below 4×10^{10} Jones and over $17.68 \text{ pW Hz}^{-1/2}$ due to the enhanced dark current. In summary, the CdS/CIGS photodiode is broadband photosensitive both in the photovoltaic and photoconductive modes, demonstrating either excellent detectivity or responsivity.

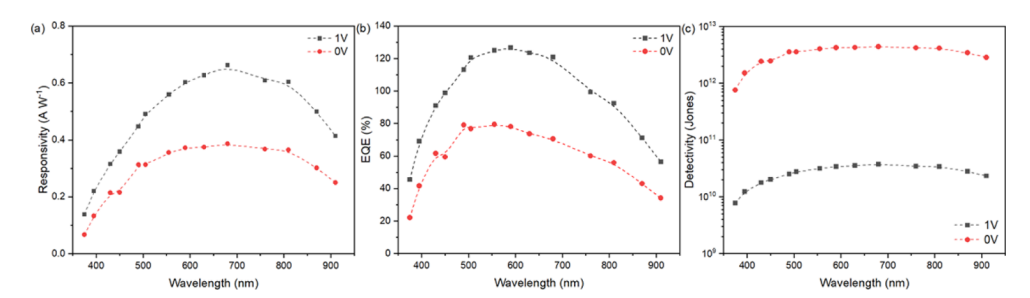


Fig. 2. (a) Responsivity, (b) EQE, and (c) Detectivity of the CdS/CIGS photodiode under $100 \, \mu \text{W cm}^{-2}$ illuminations from 375 to 910 nm with 0 V and 1 V reverse biases.

To better clarify the photoelectrical performances of the CdS/CIGS photodiode, the J-V characteristics are characterized in Fig. 3(a) under 680 nm illumination in the visible spectrum with incident light power densities varying from 20 to 500 μ W cm⁻². In Fig. 3(b), the dependence of photocurrent on the light power density under 0, 0.5 and 1 V reverse bias can be fitted by a power law:

$$I_{photo} \sim CP^{\alpha}$$
 (8)

where P is the light power density, C is a scaling constant, α is the exponent factor, which reflects the efficiency of photoexcited carriers and is ideally equal to 1 [7]. Such behavior is caused by increased photogenerated carriers with increasing incident photons from the LED illumination. In the photovoltaic mode (0 V bias), the exponent factor $\alpha \approx 1$ verifies very few trap states in the band gap and a good quality of the CdS/CIGS heterojunction [9]. However, α decreases with the increasing voltage bias to ~ 0.8 in the photoconductive mode (here 1 V reverse bias). Such sublinear behavior indicates that the photocurrent is dominated by the photoconductive mechanism [32,33]. With increasing photon flux in the photodiode, the reduced available traps result in the saturation of photocurrent, while the charge carrier photogeneration efficiency is proportional to the absorbed photon flux at a lower light density [34,35]. From the time-dependent transient photoresponse under 1 V reverse bias in Fig. 3(c), low rise and decay times of the CdS/CIGS photodiode are both estimated below 5 ms in Fig. 3(d), suggesting a stable, fast, and repeatable photoresponse of the CdS/CIGS photodiode. However, in such mode, the ratio of I_{light}/I_{dark} (~ 1.07) is quite low under 100 μ W cm^{~ 2} illumination, which can be significantly enhanced to over $\sim 10^3$ in the photovoltaic mode.

Additionally, the responsivity, EQE and detectivity of the CdS/CIGS photodiode with varying light power densities from 20 to 500 μ W cm⁻² under 0, 0.5 and 1 V reverse biases are calculated in Fig. 4(a-c). In the photovoltaic mode (0 V bias), the CdS/CIGS photodiode works as a self-driven photodiode at a light density of 20 μ W cm⁻² under 680 nm illumination and reaches a record detectivity of ~4.4×10¹² Jones and a low NEP of 0.16 μ W Hz^{-1/2}, but a relatively low responsivity of ~0.39 A W⁻¹ and an μ EQE of ~71%. In the photoconductive mode (1 V reverse bias), the CdS/CIGS photodiode demonstrates an excellent responsivity of 1.24 A W⁻¹ and an ultra-high μ EQE of 226%, but a relatively low detectivity of 7×10¹⁰ Jones and a higher μ P of 10.1 μ W Hz^{-1/2} due to the photoconductive gain mechanism. This mechanism will be discussed in detail below.

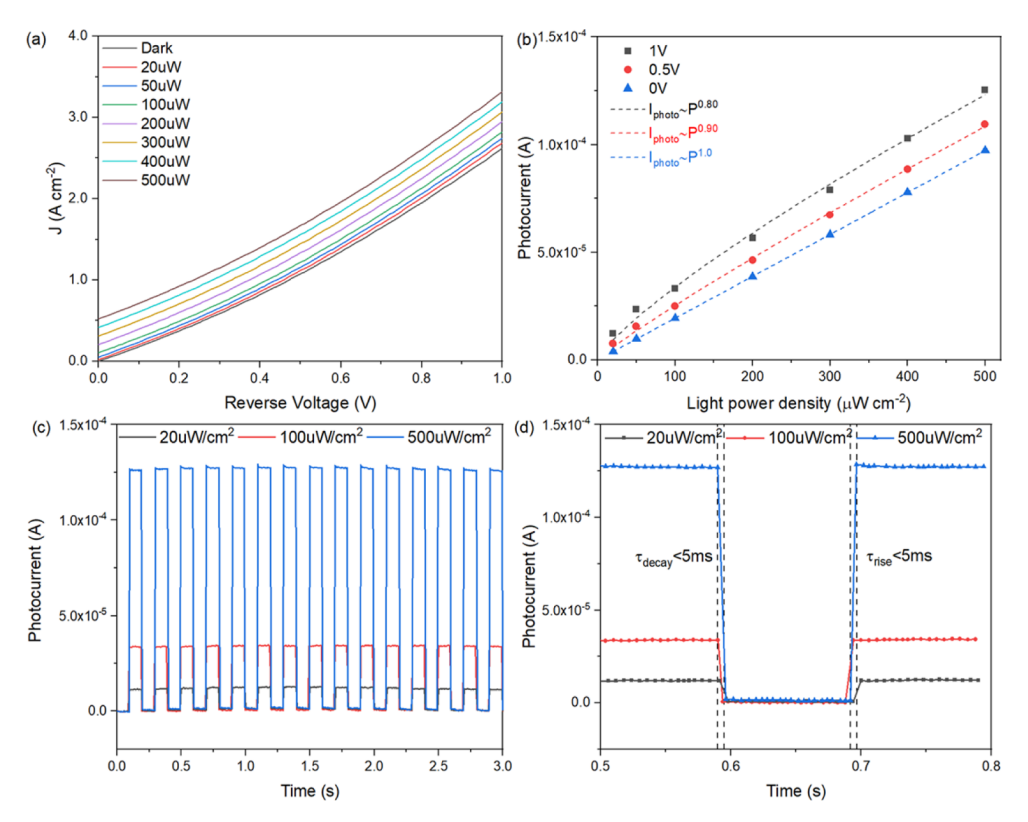


Fig. 3. (a) *J-V* curves in the dark and under 680 nm illumination at different incident light power densities. (b) Power density-dependent photocurrent fitted by power law. (c) Time-dependent transient photoresponse and (d) the rise and decay times of the photodiode under 680 nm illumination of 20, 100 and 500 $\mu W\ cm^{-2}$ with 1 V reverse bias.

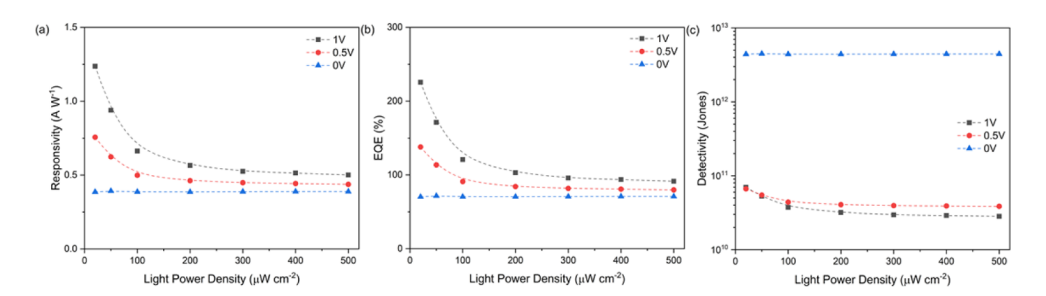


Fig. 4. (a) Responsivity, (b) EQE, and (c) detectivity of the photodiode under 680 nm illumination with 0, 0.5 and 1 V reverse biases.

Broadband photodetection is important to extend the spectral range of application for photodetectors. To further study the capability of broadband photodetection for the CdS/CIGS photodiode, the photoresponse characteristics are extended to the wavelength of 870 nm, which corresponds to the near-infrared light. The *J-V* characteristics are characterized in Fig. 5(a) under 870nm illumination with incident light power densities varying from 20 to 500 μ W cm⁻². In Fig. 5(b), the dependence of photocurrent on the light power density under 0, 0.5 and 1 V reverse bias can be fitted by the power law. In the photovoltaic mode (0 V bias), $I_{photo} \sim P^{0.98}$, approaching the ideal exponent factor of 1, implies very few trap state excitations. In the photoconductive mode (1 V reverse bias), $I_{photo} \sim P^{0.78}$, obtaining a decreased exponent factor α , is attributed to the photoconductive mechanism [32,33]. From the time-dependent transient photoresponse under 1 V reverse bias in Fig. 5(c), low rise and decay times of the CdS/CIGS photodiode are both estimated below 5 ms again in Fig. 5(d).

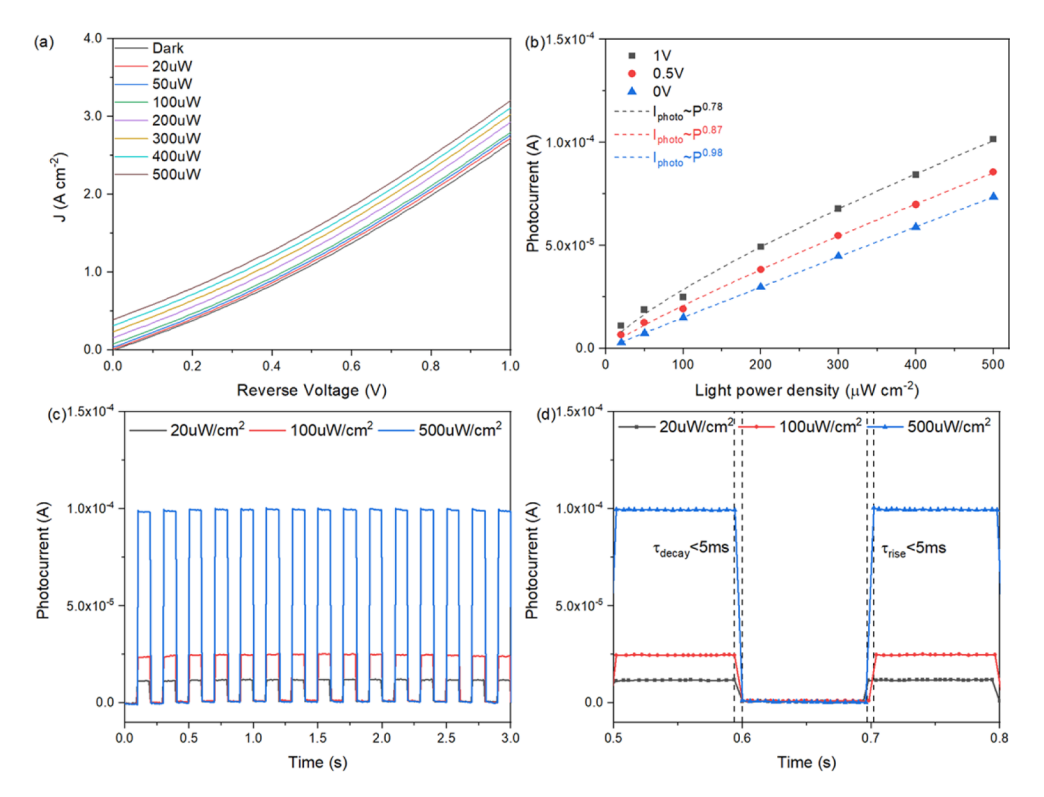


Fig. 5. (a) *J-V* curves in the dark and under 870 nm illumination at different incident light power densities. (b) Power density-dependent photocurrent fitted by power law. (c) Time-dependent transient photoresponse and (d) the rise and decay time of the photodiode under 680 nm illumination of 20, 100 and 500 μ W cm⁻² with 1 V reverse bias.

Additionally, the responsivity, EQE and detectivity of the CdS/CIGS photodiode with varying light power densities from 20 to 500 μ W cm⁻² under 0, 0.5 and 1 V reverse biases are calculated in Fig. 6(a-c) under 870nm illumination. The CdS/CIGS photodiode exhibits excellent light detection abilities under an incident light power density of 20 μ W cm⁻² in both modes. In the photovoltaic mode (0 V bias), the CdS/CIGS photodiode, working as a self-driven photodiode, reaches a high detectivity of ~3.3×10¹² Jones and a low *NEP* of 0.21 pW Hz^{-1/2}, but a relatively low responsivity of ~0.29 A W⁻¹ and an EQE of ~41%. In the photoconductive mode (1 V reverse bias), the CdS/CIGS photodiode demonstrates an excellent responsivity of 1.11 A W⁻¹

and a high EQE of 158%, but a relatively low detectivity of 6.2×10^{10} Jones and a NEP of 11.4 pW Hz^{-1/2} thanks to the photoconductive gain mechanism.

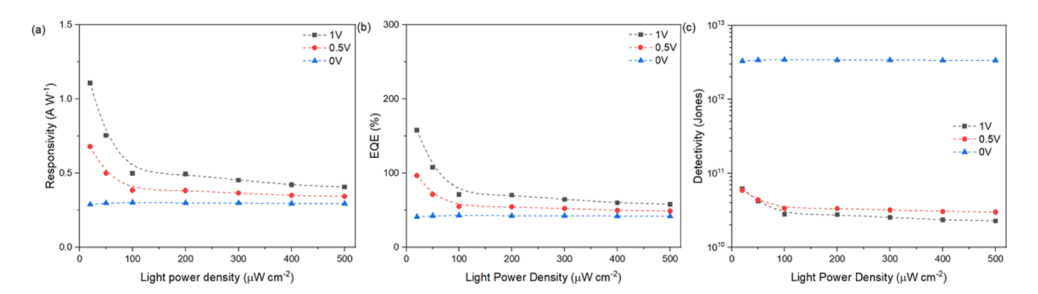


Fig. 6. (a) Responsivity, (b) *EQE*, and (c) detectivity of the photodiode under 870 nm illumination with 0, 0.5 and 1 V reverse biases.

4. Discussion

To better clarify the photodetection mechanism of the CdS/CIGS photodiode, the dependence of the ratio between the current under illumination (680 nm, 100 µW cm⁻²) and the dark current on the reverse bias is shown in Fig. 7(a). This illustrates two distinct regions with different slopes. SILVACO ATLAS numerical device simulations [23] are performed to obtain the schematic energy band diagrams in both photovoltaic mode in Fig. 7(b) and photoconductive mode in Fig. 7(c), and the electric filed distribution at 0V and 1V reverse bias in Fig. 7(d), respectively. A n-p CdS/CIGS heterojunction and a n-n CdS/ZnO interface are observed. At the CdS/CIGS heterojunction, a moderate spike-like conduction band offset (CBO) where the conduction band minimum (CBM) of CdS is higher than that of CIGS, is helpful to reduce the interfacial carrier recombination by increasing the interface recombination barrier without prohibiting the transport of photogenerated electrons from CIGS towards CdS [36,37]. Meanwhile, a large valence band offset (VBO) at the CdS/CIGS interface can reflect the photogenerated holes and reduce the interfacial carrier recombination [37]. Under low bias in Region A, the increasing dark current due to higher probability of trap-assisted tunneling and less photogenerated carriers blocked by the spike CBO with increasing bias jointly contribute to the decrease of I_{light}/I_{dark} . Next, when increasing the external bias in Region B, all the photogenerated carriers can cross the spike CBO, which causes saturation and almost constant slope of I_{light}/I_{dark} . This means that the heterojunction acts like a photoconductor rather than a photodiode in Region B [38]. Therefore, the performances of the CdS/CIGS photodiode operating in Region B can be analyzed as a pure photoconductor, taking the photoconductive gain mechanism into account.

In the photovoltaic mode illustrated in Fig. 7(b), which corresponds to Region A of Fig. 7(a), a self-driven photogeneration process is supported by effective photon absorption in CIGS absorber, photogenerated carrier separation by the built-in electrical field in space charge region (SCR), diffusion of photogenerated carriers towards quasi-neutral region (QNR), and collection of photogenerated electron-hole pairs at the contacts. In Fig. 7(c), which corresponds to Region B of Fig. 7(a), 1V reverse bias applied to the photodiode, splits the Fermi-level (E_F) into quasi-electron Fermi level (E_{FN}) and quasi-hole Fermi level (E_{FP}) due to the thermodynamic equilibrium. Applied reverse voltage (V_B) increases the p-n junction barrier by eV_B , seems to narrow the effective bandgap and enhances the electrical field density in pn junction, which is also observed from Fig. 7(d). Applying a reverse V_B of 1 V, SCR width is extended from 227.3 to 292.4 nm, as extracted from Fig. 1(d) and consistent with the simulation results in Fig. 7(d).

CIGS photodiodes show higher responsivity and impressive EQE over 100% (G > 1) in the photoconductive mode. According to the standard theory, such high gain can originate

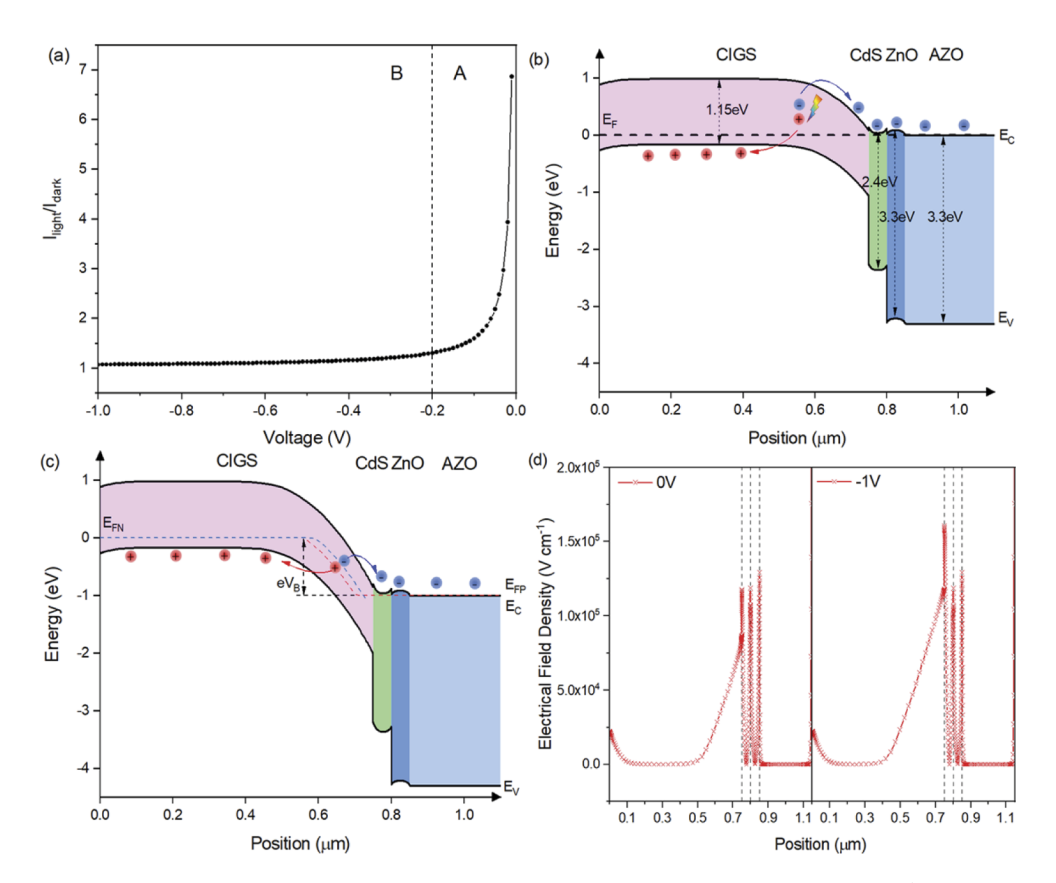


Fig. 7. (a) The ratio between the current under 680 nm illumination at 100 μ W cm⁻² and the dark current versus reverse bias. Schematic energy band diagrams of the CdS/CIGS photodiode under illumination in (b) photovoltaic (0 V bias) and (c) photoconductive mode (1 V reverse bias). (d) Electric field density distribution at 0 V and 1 V reverse bias.

from either a multiple electron-hole pair generation process from a single photon or extra charges injected from the external circuit [39]. The second hypothesis is consistent with the classical photoconductive gain mechanism especially when the incident photon energy is low. By preventing carrier recombination, this mechanism producing multiple charge carriers by one single photon, is realized by carrier recirculation after one single photon absorption. However, this classical theory remains controversial and problematic [40,41]. Therefore, in this paper, a corrected model is introduced to explain the origin of the high gain observed in our experiments.

The classical photoconductive gain model predicts the photoconductive gain (G) by [41,42]:

$$G = \tau_{life} \left(\frac{1}{\tau_{tn}} + \frac{1}{\tau_{tp}} \right) = \frac{\tau_{life}}{\tau_{tn}} \left(1 + \frac{\mu_p}{\mu_n} \right) \tag{9}$$

where τ_{life} is the minority carrier lifetime, τ_m and τ_{lp} are the free-flowing electron and hole transit times between electrodes, μ_n and μ_p are the electron and hole mobilities. Equation (9) suits both n-type and p-type semiconductors, but it is normally simplified as [30,43]:

$$G = \frac{\tau_{life}}{\tau_{transit}} \tag{10}$$

where $\tau_{transit}$ is simplified as the device transit time. Such approximation is correct only for n-type semiconductors, when μ_n is much larger than μ_p , or when τ_{tn} is much smaller than τ_{tp} .

For p-type semiconductors, G is underestimated by Eq. (10) and can be correctly estimated by Eq. (9). More specifically, photogenerated carriers could travel several times through the circuit, once the carrier transit time decreased by external electrical field gets smaller than the carrier recombination time [5,44]. In the photoconductive mode, increasing reverse bias enhances drift and diffusion velocities for free-flowing carriers and thus reduces τ_m and τ_{tp} , which can be predicted by simulation in Fig. 7(d) and calculated by [42]:

$$\tau_{tm,p} = \tau_{drift} + \tau_{diffusion} = \frac{L}{E\mu_{n,p}} + \frac{4W^2}{\pi^2 D_{n,p}}$$
 (11)

where L is the hole drift length, E is the average electrical field density in SCR, W is the diffusion length, $\mu_{n,p}$ is the electron or hole mobility, and $D_{n,p}$ is the electron or hole diffusion coefficient according to Einstein relation $(D_{n,p} = \frac{kT}{q}\mu_{n,p})$. For our device working at 1 V reverse bias, with L = 292 nm, W = 458 nm, $E = 6 \times 10^4$ V cm⁻¹, and $\mu_p = 12.5$ cm² V⁻¹ s⁻¹ in CIGS [25], τ_{tp} is estimated to be ~2.67 ns (τ_{drift} = 0.039 ns, $\tau_{diffusion}$ = 2.63 ns). Neglecting τ_{drift} due to the short drift length and the high electrical field in CdS and ZnO, with W = 300nm, and $\mu_n = 100$ cm² V⁻¹ s⁻¹ in AZO, τ_m is estimated to be ~0.14 ns. According to Eq. (9), G > 1 (EQE > 100%) can be obtained once τ_{life} is larger than $\frac{\tau_n \tau_p}{\tau_n + \tau_p} = 0.133$ ns, the measured electron lifetime in CIGS, being normally about tens of nanoseconds [45,46]. In this model, photogenerated electrons (minority carriers) can be trapped for a duration of τ_{life} due to the built-in-field in SCR and the electron traps in CIGS [39,47]. To maintain charge conservation, a hole is replenished from ZnO once a hole reaches Mo, enabling multiple holes to circulate through the circuit after one single electron-hole photogeneration [47]. Such hole injection is possibly caused by the thermionic emission or field emission when majority carriers tunnel through the junction at an ultra-high applied voltage [48]. However, in this work, the photogain exceeds 1 at a low reverse bias of 0.5 or 1 V, which can hardly cause hole tunneling. The thick CdS/CIGS heterojunction (i.e., 292.4 nm at 0 V, 227.3nm at -1 V) blocks the hole tunneling and no clear tunneling point was observed in the I-V curves. Here, the classical model mistakenly assumes a uniform distribution of photogenerated excess carriers and equal concentrations of photogenerated excess holes and electrons in semiconductor [41]. Obviously, the concentration of excess carriers in CIGS is nonuniform and voltage-dependent due to the metal-semiconductor boundary and the external bias. At the CIGS/Mo interface, the photogenerated carriers become zero since the metal doesn't generate any photocarrier. To keep continuity, the photogenerated carrier concentration has to decrease sharply near the interface. The external bias helps the photogenerated holes to drift towards the QNR in CIGS, which causes an excess hole accumulation in the QNR.

Considering the metal-semiconductor boundary and the extrinsic trapping effect from defects, surface states and depletion region, a new corrected model is given by [41]:

$$G = \frac{\tau_{n,eff}}{\tau_{transit}} \left(1 + G' \frac{\mu_p}{\mu_n} \right) \tag{12}$$

where $\tau_{n,eff}$ is the effective minority carrier lifetime, G' is defined as the gain calculated from excess carrier concentration, and μ_n is the CIGS electron mobility. In this corrected model, $\tau_{n,eff} = \overline{\Delta n}/g$, where g is the average photogeneration rate, introduces $\overline{\Delta n}$ as the average excess electron concentration to avoid the wrong assumption of uniform distribution of excess carriers. $G' = \frac{\Delta p}{\Delta n}$ considers Δp and Δn as the excess hole and electron concentrations, respectively. According to the corrected model, there are two main ways to improve the photogain of a photodetector. Firstly, if μ_p is larger than μ_n , the photogain can be improved but always stays lower than the ratio of the majority to minority mobilities [41]. However, experimentally, it's hard to reach a higher μ_p than μ_n for a p-type semiconductor such as CIGS. Secondly, G' can be enhanced to over 1, once $\Delta n < \Delta p$. If the semiconductor is perfect without any defects and surface

states, G' is equal to 1. However, with defects and surface states, excess minority electrons might be trapped in the defects, surface states and depletion region, while the same number of holes are left in the CdS/CIGS photodiode [40]. In such case, the number of excess holes becomes higher than that of electrons, which causes G'>1 and thus G>1 (EQE>100%). However, with increasing light density, available trap states would be gradually saturated, which makes the extra electron-hole pairs recombine immediately and prevent the photoconductive gain process [49]. Therefore, photoconductive gain mechanism is more pronounced at a lower incident light density under higher bias voltage.

The optoelectrical performances of the as-fabricated CdS/CIGS photodiode in this work are summarized and compared to other recently reported CIGS- or CdS-based heterojunction photodiodes in Table 1. The K-doped CIGS shows the highest responsivity but is designed specifically for the near-infrared photodetection [11]. Compared to other broadband CdS/CIGS photodiodes, our ultra-thin photodiode with the thinnest reported CIGS film of 750 nm for photodetectors, exhibits outstanding performances while working at both photovoltaic and photoconductive mode. Under 0 V bias, the as-fabricated photodiode indicates a record detectivity, which is 139% higher than the best reported detectivity for CdS/CIGS photodetectors [9]. Under 1 V reverse bias, excellent responsivity and *EQE* are 4% and 25% higher, respectively, than the reported highest values for broadband CdS/CIGS photodetectors [10]. Meanwhile, relatively low predicted rise and decay times, lower than 5 ms, are obtained. Compared to other CdS-based heterojunction photodiodes, CdS/CIGS photodiode in this work shows obviously higher responsivity and EQE, as well as competitive detectivity and response times [50–52].

Table 1. Comparison with previously reported CIGS- or CdS-based heterojunction photodiodes

Structure	Measured Conditions ^a	$R [A W^{-1}]$	EQE	D [Jones]	Rise/Decay Times [ms]	Refs.
CdS/Al ₂ O ₃ /CIGS	PV (0 V, λ=800 nm)	0.54	~90%	1.84×10^{12}	0.003/0.006	[9]
Flexible CdS/CIGS	PC (-2 V, <i>λ</i> =808 nm)	1.18	181% ^b	6.65×10^{10}	70/88	[10]
CdS/K-doped CIGS	PV (0 V, λ=980 nm)	~0.35	~45%	~1×10 ¹⁰	/	[11]
	PC (-0.4 V, <i>λ</i> =980 nm)	1.87	237%	6.45×10^{10}	20/20	
CdS/Se	PV (0V, λ=500 nm)	0.04	9.9% ^b	1.3×10 ¹³	0.002/22	[50]
Flexible CdS/Si	PV (0V, λ=325 nm)	0.0046	1.8% ^b	1×10 ¹²	245/277	[51]
CdS/SnS	PV (0V, λ=650 nm)	0.0104	2%	3.56×10^{11}	<30	[52]
CdS/CIGS	PV (0V, λ=680 nm)	~0.39	~71%	~4.4×10 ¹²	/	This work
	PC (-1V, <i>λ</i> =680 nm)	1.24	226%	7×10^{10}	<5/<5	

^aThe photovoltaic and photoconductive modes are abbreviated as PV and PC, respectively.

5. Conclusions

In this work, a high-performance ultra-thin CdS/CIGS heterojunction photodiode, fabricated on steel, firstly exhibits dual-mode broadband photodetection from UV to near-infrared spectrum, reaching both high responsivity and detectivity by switching the detection modes of the device. From 395 to 910 nm, excellent responsivities over 0.4 A W⁻¹ and impressive *EQE*s over 100% are observed in the photoconductive mode (1 V reverse bias), while high detectivities over 2×10^{12} Jones are obtained in the photovoltaic mode (0V). Importantly, the CdS/CIGS photodiode shows its best performances under an incident light power of 20 μ W cm⁻². Operating in the photovoltaic mode as a self-driven photodetector without external energy consumption, the photodiode reaches a record detectivity of $\sim4.4\times10^{12}$ Jones, a low noise equivalent power (*NEP*) of 0.16 pW Hz^{-1/2}, and a high I_{light}/I_{dark} ratio of over $\sim10^3$ at 680 nm illumination. Working in the photoconductive

^bThis value is not obtained from the literature but calculated from Eq. (7).

mode, the photodiode reaches a significantly enhanced responsivity of 1.24 A W^{-1} and an impressive EQE of 226%. By SILVACO ATLAS simulation and theoretical analysis, a moderate spike-like CBO and a large VBO help to reduce the interfacial carrier recombination. In the photovoltaic mode, the responsivity and EQE of the photodiode are both limited due to the lack of an effective photoconductive gain mechanism. According to the corrected gain mechanism, EQE over 100% can originate from the difference between photogenerated excess hole and electron concentrations in the device, caused by the trapped minority electrons in the defects, surface states and depletion region. These superior results indicate that the CdS/CIGS heterojunction photodiode is a promising photodetector to balance the responsivity and detectivity in a single device. Finally, the steel substrate offers the possibility to further study its flexible performances for potential portable applications.

Funding. China Scholarship Council and Université Catholique de Louvain Co-Funding Fellowship (CSC2018 06130158); EU H2020 Research and Innovation Program (720887); National Natural Science Foundation of China (62004065); Natural Science Foundation of Hunan Province (2020JJ5087).

Disclosures. The authors declare no conflicts of interest.

Data availability. Data underlying the results presented in this paper are not publicly available at this time but may be obtained from the authors upon reasonable request.

References

- X. Gong, M. Tong, Y. Xia, W. Cai, J. S. Moon, Y. Cao, G. Yu, C. L. Shieh, B. Nilsson, and A. J. Heeger, "High-detectivity polymer photodetectors with spectral response from 300 nm to 1450 nm," Science 325(5948), 1665–1667 (2009).
- F. H. L. Koppens, T. Mueller, P. Avouris, A. C. Ferrari, M. S. Vitiello, and M. Polini, "Photodetectors based on graphene, other two-dimensional materials and hybrid systems," Nat. Nanotechnol. 9(10), 780–793 (2014).
- Z. Xu, S. Lin, X. Li, S. Zhang, Z. Wu, W. Xu, Y. Lu, and S. Xu, "Monolayer MoS₂/GaAs heterostructure self-driven photodetector with extremely high detectivity," Nano Energy 23, 89–96 (2016).
- M. Kielar, T. Hamid, M. Wiemer, F. Windels, L. Hirsch, P. Sah, and A. K. Pandey, "Light detection in open-circuit voltage mode of organic photodetectors," Adv. Funct. Mater. 30(9), 1907964 (2020).
- M. I. Saidaminov, M. A. Haque, M. Savoie, A. L. Abdelhady, N. Cho, I. Dursun, U. Buttner, E. Alarousu, T. Wu, and O. M. Bakr, "Perovskite photodetectors operating in both narrowband and broadband regimes," Adv. Mater. 28(37), 8144–8149 (2016).
- H. Qiao, Z. Huang, X. Ren, S. Liu, Y. Zhang, X. Qi, and H. Zhang, "Self-powered photodetectors based on 2D materials," Adv. Opt. Mater. 8(1), 1900765 (2020).
- H. Luo, B. Wang, E. Wang, X. Wang, Y. Sun, Q. Li, S. Fan, C. Cheng, and K. Liu, "Phase-transition modulated, high-performance dual-mode photodetectors based on WSe₂/VO₂ heterojunctions," Appl. Phys. Rev. 6(4), 041407 (2019)
- L. Chen, W. Tian, L. Min, F. Cao, and L. Li, "Si/CuIn_{0.7}Ga_{0.3}Se₂ core–shell heterojunction for sensitive and self-driven UV–VIS–NIR broadband photodetector," Adv. Opt. Mater. 7(10), 1900023 (2019).
- Y. Yuan, L. Zhang, G. Yan, G. Cen, Y. Liu, L. Zeng, C. Zeng, C. Zhao, R. Hong, and W. Mai, "Significantly enhanced detectivity of CIGS broadband high-speed photodetectors by grain size control and ALD-Al₂O₃ interfacial-layer modification," ACS Appl. Mater. Interfaces 11(22), 20157–20166 (2019).
- S. Qiao, J. Liu, X. Niu, B. Liang, G. Fu, Z. Li, S. Wang, K. Ren, and C. Pan, "Piezophototronic effect enhanced photoresponse of the flexible Cu(In,Ga)Se₂ (CIGS) heterojunction photodetectors," Adv. Funct. Mater. 28(19), 1707311 (2018).
- 11. J. H. Kim, H. Han, M. K. Kim, J. Ahn, D. K. Hwang, T. J. Shin, B. K. Min, and J. A. Lim, "Solution-processed near-infrared Cu(In,Ga)(S,Se)₂ photodetectors with enhanced chalcopyrite crystallization and bandgap grading structure via potassium incorporation," Sci. Rep. **11**(1), 7820 (2021).
- Z. Zhang, S. Qiao, J. Liu, L. Guo, Z. Li, L. Yang, S. Wang, and G. Fu, "Lateral photocurrent-induced high-performance self-powered photodetector observed in CIGS heterojunction," IEEE Trans. Electron Devices 67(4), 1639–1644 (2020).
- S. Qiao, K. Feng, Z. Li, G. Fu, and S. Wang, "Ultrahigh, ultrafast and large response size visible-near-infrared optical position sensitive detectors based on CIGS structures," J. Mater. Chem. C 5(20), 4915–4922 (2017).
- X. Zeng, J. Lontchi, M. Zhukova, L. Fourdrinier, I. Qadir, Y. Ren, E. Niemi, G. Li, and D. Flandre, "High-responsivity broadband photodetection of an ultra-thin In₂S₃/CIGS heterojunction on steel," Opt. Lett. 46(10), 2288–2291 (2021).
- A. Chirilă, S. Buecheler, F. Pianezzi, P. Bloesch, C. Gretener, A. R. Uhl, C. Fella, L. Kranz, J. Perrenoud, S. Seyrling, R. Verma, S. Nishiwaki, Y. E. Romanyuk, G. Bilger, and A. N. Tiwari, "Highly efficient Cu(In,Ga)Se₂ solar cells grown on flexible polymer films," Nat. Mater. 10(11), 857–861 (2011).
- R. Wuerz, A. Eicke, M. Frankenfeld, F. Kessler, M. Powalla, P. Rogin, and O. Yazdani-Assl, "CIGS thin-film solar cells on steel substrates," Thin Solid Films 517(7), 2415–2418 (2009).

- L. Zortea, S. Nishiwaki, T. P. Weiss, S. Haass, J. Perrenoud, L. Greuter, T. Feurer, G. Palaniswamy, S. Buecheler, and A. N. Tiwari, "Cu(In,Ga)Se₂ solar cells on low cost mild steel substrates," Sol. Energy 175, 25–30 (2018).
- 18. P. Salomé, V. Fjällström, A. Hultqvist, and M. Edoff, "Na doping of CIGS solar cells using low sodium-doped Mo layer," IEEE J. Photovoltaics 3(1), 509–513 (2013).
- F. Pianezzi, P. Reinhard, A. Chirilă, B. Bissig, S. Nishiwaki, S. Buecheler, and A. N. Tiwari, "Unveiling the effects of post-deposition treatment with different alkaline elements on the electronic properties of CIGS thin film solar cells," Phys. Chem. Chem. Phys. 16(19), 8843–8851 (2014).
- R. Carron, S. Nishiwaki, T. Feurer, R. Hertwig, E. Avancini, J. Löckinger, S. C. Yang, S. Buecheler, and A. N. Tiwari, "Advanced alkali treatments for high-efficiency Cu(In,Ga)Se₂ solar cells on flexible substrates," Adv. Energy Mater. 9(24), 1900408 (2019).
- 21. K. Kim, I. Jeong, Y. Cho, D. Shin, S. Song, S. K. Ahn, Y. J. Eo, A. Cho, C. Jung, W. Jo, J. H. Kim, P. P. Choi, J. Gwak, and J. H. Yun, "Mechanisms of extrinsic alkali incorporation in CIGS solar cells on flexible polyimide elucidated by nanoscale and quantitative analyses," Nano Energy 67, 104201 (2020).
- 22. M. Burgelman, K. Decock, A. Niemegeers, J. Verschraegen, and S. Degrave, SCAPS Manual (2018).
- 23. Silvaco, Inc., Atlas User's Manual (2018).
- S. S. Hegedus and W. N. Shafarman, "Thin-film solar cells: Device measurements and analysis," Prog. Photovoltaics 12(23), 155–176 (2004).
- 25. J. Lontchi, M. Zhukova, M. Kovacic, J. Krc, W. C. Chen, M. Edoff, S. Bose, P. M. P. Salome, J. Goffard, A. Cattoni, L. Gouillart, S. Collin, V. Gusak, and D. Flandre, "Optimization of back contact grid size in Al₂O₃-rear-passivated ultrathin CIGS PV cells by 2-D simulations," IEEE J. Photovoltaics 10(6), 1908–1917 (2020).
- 26. J. M. V. Cunha, C. Rocha, C. Vinhais, P. A. Fernandes, and P. M. P. Salome, "Understanding the AC equivalent circuit response of ultrathin Cu(In,Ga)Se₂ solar cells," IEEE J. Photovoltaics **9**(5), 1442–1448 (2019).
- 27. J. M. V. Cunha, K. Oliveira, J. Lontchi, T. S. Lopes, M. A. Curado, J. R. S. Barbosa, C. Vinhais, W. C. Chen, J. Borme, H. Fonseca, J. Gaspar, D. Flandre, M. Edoff, A. G. Silva, J. P. Teixeira, P. A. Fernandes, and P. M. P. Salomé, "High-performance and industrially viable nanostructured SiO_x layers for interface passivation in thin film solar cells," Sol. RRL 5(3), 2000534 (2021).
- L. Zhang, P. Wan, T. Xu, C. Kan, and M. Jiang, "Flexible ultraviolet photodetector based on single ZnO microwire/polyaniline heterojunctions," Opt. Express 29(12), 19202–19213 (2021).
- Q. Qiu and Z. Huang, "Photodetectors of 2D Materials from Ultraviolet to Terahertz Waves," Adv. Mater. 33(15), 2008126 (2021).
- 30. J. Jiang, X. Zou, Y. Lv, Y. Liu, W. Xu, Q. Tao, Y. Chai, and L. Liao, "Rational design of Al₂O₃/2D perovskite heterostructure dielectric for high performance MoS₂ phototransistors," Nat. Commun. **11**(1), 4266 (2020).
- X. Liu, S. Hu, J. Luo, X. Li, J. Wu, D. Chi, K. W. Ang, W. Yu, and Y. Cai, "Suspended MoS2 Photodetector Using Patterned Sapphire Substrate," Small 17(43), 2100246 (2021).
- 32. M. Zhao, J. Su, Y. Zhao, P. Luo, F. Wang, W. Han, Y. Li, X. Zu, L. Qiao, and T. Zhai, "Sodium-mediated epitaxial growth of 2D ultrathin Sb₂Se₃ flakes for broadband photodetection," Adv. Funct. Mater. **30**(13), 1909849 (2020).
- 33. Z. Ma, S. Chai, Q. Feng, L. Li, X. Li, L. Huang, D. Liu, J. Sun, R. Jiang, T. Zhai, and H. Xu, "Chemical vapor deposition growth of high crystallinity Sb₂Se₃ nanowire with strong anisotropy for near-infrared photodetectors," Small 15(9), 1805307 (2019).
- 34. C. Soci, A. Zhang, B. Xiang, S. A. Dayeh, D. P. R. Aplin, J. Park, X. Y. Bao, Y. H. Lo, and D. Wang, "ZnO nanowire UV photodetectors with high internal gain," Nano Lett. 7(4), 1003–1009 (2007).
- 35. X. Liu, L. Gu, Q. Zhang, J. Wu, Y. Long, and Z. Fan, "All-printable band-edge modulated ZnO nanowire photodetectors with ultra-high detectivity," Nat. Commun. 5(1), 4007 (2014).
- 36. G. S. Park, V. Ben Chu, B. W. Kim, D. W. Kim, H. S. Oh, Y. J. Hwang, and B. K. Min, "Achieving 14.4% alcohol-based solution-processed Cu(In,Ga)(S,Se)₂ thin film solar cell through interface engineering," ACS Appl. Mater. Interfaces 10(12), 9894–9899 (2018).
- 37. R. Wang, M. Lan, Y. Zheng, J. Yang, B. Li, and S. H. Wei, "Interface engineering of Cu(In,Ga)Se₂ solar cells by optimizing Cd- and Zn-chalcogenide alloys as the buffer layer," ACS Appl. Mater. Interfaces 13(13), 15237–15245 (2021).
- 38. H. Manis-Levy, R. Shikler, Y. Golan, and G. Sarusi, "High photoconductive gain in a GaAs/PbS heterojunction based SWIR detector," Appl. Phys. Lett. 117(8), 081107 (2020).
- X. Li, J. E. Carey, J. W. Sickler, M. U. Pralle, C. Palsule, and C. J. Vineis, "Silicon photodiodes with high photoconductive gain at room temperature," Opt. Express 20(5), 5518–5523 (2012).
- K. Chen, X. Zhao, A. Mesli, Y. He, and Y. Dan, "Dynamics of charge carriers in silicon nanowire photoconductors revealed by photo hall effect measurements," ACS Nano 12(4), 3436–3441 (2018).
- 41. Y. Dan, X. Zhao, K. Chen, and A. Mesli, "A photoconductor intrinsically has no gain," ACS Photonics 5(10), 4111–4116 (2018).
- 42. S.M. Sze and K.K. Ng, Physics of Semiconductor Devices (2006).
- 43. J. Wang, A. Rousseau, E. Eizner, A. L. Phaneuf-L'Heureux, L. Schue, S. Francoeur, and S. Kéna-Cohen, "Spectral responsivity and photoconductive gain in thin film black phosphorus photodetectors," ACS Photonics 6(12), 3092–3099 (2019).

- R. Dong, Y. Fang, J. Chae, J. Dai, Z. Xiao, Q. Dong, Y. Yuan, A. Centrone, X. C. Zeng, and J. Huang, "High-gain and low-driving-voltage photodetectors based on organolead triiodide perovskites," Adv. Mater. 27(11), 1912–1918 (2015).
- 45. S. Karki, P. Paul, G. Rajan, B. Belfore, D. Poudel, A. Rockett, E. Danilov, F. Castellano, A. Arehart, and S. Marsillac, "Analysis of recombination mechanisms in RbF-treated cigs solar cells," IEEE J. Photovoltaics 9(1), 313–318 (2019).
- 46. I. L. Repins, W. K. Metzger, C. L. Perkins, J. V. Li, and M. A. Contreras, "Correlation between measured minority-carrier lifetime and Cu(In,Ga)Se₂ device performance," IEEE Trans. Electron Devices 57(11), 2957–2963 (2010).
- 47. G. Konstantatos, M. Badioli, L. Gaudreau, J. Osmond, M. Bernechea, F. P. G. De Arquer, F. Gatti, and F. H. L. Koppens, "Hybrid graphene-quantum dot phototransistors with ultrahigh gain," Nat. Nanotechnol. 7(6), 363–368 (2012).
- 48. M. Liao, X. Wang, T. Teraji, S. Koizumi, and Y. Koide, "Light intensity dependence of photocurrent gain in single-crystal diamond detectors," Phys. Rev. B 81(3), 033304 (2010).
- 49. D. Shao, J. Gao, P. Chow, H. Sun, G. Xin, P. Sharma, J. Lian, N. A. Koratkar, and S. Sawyer, "Organic-inorganic heterointerfaces for ultrasensitive detection of ultraviolet light," Nano Lett. 15(6), 3787–3792 (2015).
- J. Wang, Y. Chang, L. Huang, K. Jin, and W. Tian, "Designing CdS/Se heterojunction as high-performance self-powered UV-visible broadband photodetector," APL Mater. 6(7), 076106 (2018).
- 51. Y. Dai, X. Wang, W. Peng, C. Xu, C. Wu, K. Dong, R. Liu, and Z. L. Wang, "Self-Powered Si/CdS Flexible Photodetector with Broadband Response from 325 to 1550 nm Based on Pyro-phototronic Effect: An Approach for Photosensing below Bandgap Energy," Adv. Mater. 30(9), 1705893 (2018).
- 52. Y. Chang, J. Wang, F. Wu, W. Tian, and W. Zhai, "Structural Design and Pyroelectric Property of SnS/CdS Heterojunctions Contrived for Low-Temperature Visible Photodetectors," Adv. Funct. Mater. 30(23), 2001450 (2020).